https://doi.org/10.5194/amt-2021-246
Preprint. Discussion started: 28 September 2021

Atmospheric Measurement Techniques Discussions
Open Access

Radiation correction and uncertainty evaluation of RS41 temperature sensors by using an upper-air simulator

Sang-Wook Lee[1,2], Sunghun Kim[1], Young-Suk Lee[1], Byung Il Choi[1], Woong Kang[1], Youn Kyun Oh[1], Seongchong Park[1], Jae-Keun Yoo[1], Sungjun Lee[1], Suyong Kwon[1,2], Yong-Gyoo Kim[1]

[1]Division of Physical Metrology, Korea Research Institute of Standards and Science, Daejeon 34113, Republic of Korea
[2]Department of Science of Measurement, University of Science and Technology, Daejeon 34113, Republic of Korea

Correspondence to: Y.-G. Kim (dragon@kriss.re.kr)

Abstract. An upper-air simulator (UAS) has been developed at the Korea Research Institute of Standards and Science (KRISS) to study the effects of solar irradiation of commercial radiosondes. In this study, the uncertainty of the radiation correction of a Vaisala RS41 temperature sensor is evaluated using the UAS at KRISS. First, the effects of environmental parameters including the temperature (T), pressure (P), ventilation speed (v), and irradiance (S) are formulated in the context of the radiation correction. The considered ranges of T, P, and v are –67 to 20 °C, 5−500 hPa, and 4−7 m·s^{-1}, respectively, with a fixed S_0 = 980 W·m^{-2}. Second, the uncertainties in the environmental parameters determined using the UAS are evaluated to calculate their contribution to the uncertainty in the radiation correction. In addition, the effects of rotation and tilting of the sensor boom with respect to the irradiation direction are investigated. The uncertainty in the radiation correction is obtained by combining the contributions of all uncertainty factors. The expanded uncertainty associated with the radiation correction for the RS41 temperature sensor is 0.119 °C at the coverage factor k = 2 (approximately 95% confidence level). The findings obtained by reproducing the environment of the upper air by using the ground-based facility can provide a basis to increase the measurement accuracy of radiosondes within the framework of traceability to the International System of Units.

https://doi.org/10.5194/amt-2021-246
Preprint. Discussion started: 28 September 2021

1 Introduction

The measurement of temperature and humidity in the free atmosphere is of significance for weather prediction, climate monitoring, and aviation safety assurance. Radiosondes are telemetry devices that include various sensors to measure data that are transmitted to a ground receiver while the device is carried by a weather balloon to an altitude of approximately 35 km. Since their development in the 1930s, radiosondes have been widely used to measure various essential climate variables (ECVs) such as the temperature, water vapour, wind speed, and wind direction in the upper-air atmosphere. Owing to their high accuracy, radiosonde measurements provide reference for other remote sensing techniques such as those based on satellite and lidar. Notably, an effective method to evaluate the measurement accuracy specified by manufacturers remains to be specified. The dependence of accuracy evaluation based only on manufacturer data may lead to inhomogeneity among users, including upper-air observatories that use different radiosonde models.

To ensure the quality control of measurements in the upper air, the Global Climate Observing System (GCOS) Reference Upper-Air Network (GRUAN) was founded in 2008. The key objective of the GRUAN is to perform high quality measurements of the ECVs from the surface to the stratosphere to monitor climate change. To this end, the required temperature measurement accuracy in the troposphere and stratosphere has been specified as 0.1 K and 0.2 K, respectively (Gcos, 2007).

The main source of error in the temperature measured by radiosondes is solar radiation during sounding in daytime. The temperature sensors of most commercial radiosondes are exposed to solar radiation, and the radiative heating increases the temperature to more than the air temperature. Correcting the radiation effect is challenging because the temperature of sensors is also affected by other thermal exchange processes such as conduction from the sensor boom, convective cooling by air ventilation, and long-wave radiation from sensors. To minimize the effect of radiative heating of radiosonde temperature sensors, the size of sensors has been reduced. Moreover, the sensor boom has been redesigned to reduce the thermal conduction to sensors. However, it is not possible to eliminate the combined effect of solar irradiation.

Many researchers have attempted to correct the radiation effect on radiosonde temperature sensors through theoretical and experimental techniques. The early theoretical approaches were based on heat transfer equations governing the thermal exchange between the sensor and surrounding media (Luers, 1990; Mcmillin et al., 1992). However, the application of these approaches requires complete knowledge regarding the material properties of the sensor and sensor boom and air characteristics in a wide range of temperatures, and the aerodynamic characteristics for a specific sensor geometry must be determined.

A few researchers performed in-flight experiments to derive a formula to correct the radiation effect (Schmidlin et al., 1986). A correction formula was derived by establishing the relationship between the irradiance and increase in the temperature via radiative heating during daytime sounding (Philipona et al., 2013). Two identical thermocouples were used to measure the temperature difference when only one sensor was exposed to solar radiation and the other was shielded. However, the effect of the shield could not be eliminated.

https://doi.org/10.5194/amt-2021-246
Preprint. Discussion started: 28 September 2021

Other groups adopted a chamber system for radiation correction by simulating the upper-air environments including the solar radiation. The GRUAN conducted experiments by using a chamber that could imitate the pressure, air ventilation, and solar irradiance by using a vacuum pump, fan, and lamp or sunlight, respectively (Dirksen et al., 2014). Recently, the same group conducted experiments by using a new laboratory setup including a wind tunnel with various functionalities and improved uncertainties in processing the GRUAN data for the Vaisala RS41 sensors (personal correspondence). However, these experiments were conducted at room temperature, and thus, the temperature effect on the sensors was not considered. Notably, the existing studies based on other chamber systems reported that the solar-irradiation-induced temperature rise of sensors increases as the air temperature is decreased (Lee et al., 2018a; Lee et al., 2020).

Recently, the Korea Research Institute of Standards and Science (KRISS) developed an upper-air simulator (UAS) that can simultaneously control the temperature, pressure, air ventilation, and irradiation (Lee et al., 2020). This UAS has been also used to calibrate the relative humidity sensors of commercial radiosondes at low temperatures (down to −67 °C) (Lee et al., 2021).

In this study, the uncertainty in the radiation correction of a Vaisala RS41 temperature sensor is evaluated using the UAS at KRISS. The layout of the UAS is described in Section 2, along with the addition of new functions to consider the effect of the rotation and tilting of the sensor. As described in Section 3, a radiation correction formula for the RS41 sensor is derived through a series of experiments involving varying temperature (T), pressure (P), and ventilation speed (v) values in the following ranges: –67 to 20 °C, 5−500 hPa, and 4−7 m·s^{-1}, respectively, with a fixed irradiance S_0 = 980 W·m^{-2}. The effects of sensor rotation and tilting with respect to the incident irradiation are also investigated. Section 4 describes the evaluation of the uncertainties associated with the environmental parameters and sensor motions/positions controlled in the UAS to calculate the contribution of these factors to the uncertainty in the radiation correction. This study can help enhance the measurement accuracy of radiosondes within the framework of traceability to the International System of Units (SI) by providing a methodology for radiation correction in an environment similar to that which may be encountered by radiosondes.

2 Layout of the UAS

2.1 Temperature control of the radiosonde test chamber by using a climate chamber

Figure 1(a) shows the test chamber of the UAS with an installed radiosonde for the radiation correction. The test chamber is inside a climate chamber (Tenney environmental, Model: C64RC) to control the temperature. The working space of the climate chamber is sized 1219 mm × 1219 mm × 1219 mm. The radiosonde is installed upside-down, as shown in Fig. 1(b), and the air flows into the test chamber from the bottom. The air is precooled before being supplied to the test chamber by passing it through a heat exchanger submerged in a thermostatic bath (Kambic metrology, Model: OB-50/2 ULT). The temperature of the test chamber is measured using a calibrated platinum resistance thermometer (PRT).

2.2 Pressure and ventilation speed control through sonic nozzles and a vacuum pump

To control the air ventilation speed at low pressures, sonic nozzles, also known as critical flow Venturi, are used. The sonic nozzles are fabricated as toroidal-throat Venturi nozzles to comply with the ISO 9300 standard (Iso, 2005) and calibrated using low-pressure gas flow standard system at KRISS (Choi et al., 2010). Sonic nozzles can be used to achieve a specific maximum constant flow when the ratio of the downstream pressure (P_e) to the upstream pressure (P_o) is smaller than a certain critical point ($P_e/P_o < P_c/P_o$). The test chamber lies in the downstream region of the sonic nozzles, in which the pressure is lowered using a vacuum pump (WONVAC, Model: WOVP-0600) to attain the critical condition. Six sonic nozzles with different throat diameters are used to generate air ventilation speeds ranging from 4 $m \cdot s^{-1}$ to 7 $m \cdot s^{-1}$ in the pressure range of 5–500 hPa. The generated air flow is measured through laser Doppler velocimetry to investigate the spatial gradient in the test chamber.

2.3 Irradiation control by using a solar simulator

Solar irradiation is imitated by using a solar simulator with a xenon DC arc lamp (Newport, Model: 66926-1000XF-R07). The virtual sunlight is irradiated onto the radiosonde temperature sensor and the sensor boom through quartz windows of the test chamber. A constant irradiance of 980 $W \cdot m^{-2}$ is adopted throughout this study. The two-dimensional distribution of the irradiance is recorded at the radiosonde sensor location by using a calibrated Si photodiode (Thorlabs, Model: SM05PD2A). The spatial uniformity of the irradiance around the sensor position is within ±5%. In addition, the irradiance is monitored to check its drift during the experiments by using a photodiode-based pyranometer (Apogee, Model: SP-110-SS) installed behind the test chamber. The pyranometer is calibrated at KRISS.

2.4 Installation of RS41

As a proof of concept, the uncertainty associated with the radiation correction for a commercial radiosonde (Vaisala, RS41) is evaluated using the UAS. A complete RS41 unit including the sensor boom, antenna, and main body is installed upside-down in the test chamber, as shown in Figs. 1(a) and (b). The sensor boom is placed parallel to the air flow (blue dashed arrows). The sensor boom is irradiated (red dotted arrows) by the solar simulator in a perpendicular manner through quartz windows (50 mm × 70 mm). The temperature recorded by the RS41 is collected through remote data transmission as in the case of soundings by the Vaisala sounding system MW41. It seems that the radiation correction by the manufacturer is applied only during the sounding state. The RS41 unit remains at the pre-sounding state in the manual sounding mode throughout the data acquisition, and thus, raw temperature with no radiation correction is obtained.

2.5 Rotation and tilting of the sensor boom

A radiosonde exhibits continuous movements such as pendulum and rotational motions during sounding. Thus, the angle of the sensor boom with respect to the radiation direction or air flow may constantly vary. To consider this aspect, the UAS is

https://doi.org/10.5194/amt-2021-246
Preprint. Discussion started: 28 September 2021

modified to be able to simulate these situations through rotating and tilting of the sensor boom in the test chamber. Figures 1(c)–(e) illustrate the mechanisms in the test chamber that enable the (d) rotation of the radiosonde around the vertical axis and (e) tilting of the sensor boom from the (c) normal position. The rotation cycle and tilt are controlled using stepper motors. Rotation cycles of 5 s, 10 s, and 15 s are considered. The maximum tilt is 27° with respect to the vertical axis. Effects of the rotation and incident angle of irradiation are studied and incorporated in the uncertainty evaluation of the radiation correction of the sensor.

2 Experiment Details

3.1 Effect of pressure

The temperature rise due to irradiation (ΔT_{rad}) is defined as the difference in the temperatures with irradiation (T_{on}) and without irradiation (T_{off}); $\Delta T_{rad} = T_{on} - T_{off}$. It has been reported that ΔT_{rad} significantly increases as the pressure (P) decreases from 100 hPa to 7 hPa in the UAS (Lee et al., 2020). This phenomenon occurs because the convective cooling process is weakened as the air density decreases at low pressures. In this study, the pressure range is extended (5−500 hPa) to formulate the corresponding effect at a more practical scale. Figures 2(a) and (b) show ΔT_{rad} as a function of pressure from 5 hPa to 50 hPa and from 50 hPa to 500 hPa, respectively. The pressure effect is demonstrated in two ranges because the effect of T is well distinguished at the low-pressure range, as shown in Fig. 2(a), whereas it is not clearly observable in the high pressure range, as shown in Fig. 2(b). This phenomenon can be attributed to the relatively larger uncertainties in ΔT_{rad} at high pressures in the UAS. Therefore, ΔT_{rad} at each temperature is fitted individually by using an empirical exponential function, indicated by dashed lines in Fig. 2(a). The mean of ΔT_{rad} for the considered temperature range (−67 °C to 20 °C) is fitted using a single exponential function, indicated by a dashed line in Fig. 2(b). The fitting equations represented in Fig. 2(a) are exponential functions:

$$\Delta T_{rad} = T_0(T) + A_0(T)\cdot\exp(-P/P_0(T)) \quad \text{for } 5\text{ hPa} \le P \le 50\text{ hPa},\ S_0 = 980\ \mathrm{W\cdot m^{-2}}\ , \tag{1}$$

where $T_0(T)$, $A_0(T)$, and $P_0(T)$ are fitting coefficients with functions of T, having units of °C, °C, and hPa, respectively. The irradiation intensity S_0 is set as 980 W·m^{-2} throughout this study.

In addition, the fitting equation represented in Fig. 2(b) is an exponential function:

$$\Delta T_{rad} = T_1 + A_1\cdot\exp(-P/P_1) \qquad \text{for } 50\text{ hPa} < P < 500\text{ hPa},\ S_0 = 980\ \mathrm{W\cdot m^{-2}}\ , \tag{2}$$

where T_1, A_1, and P_1 are fitting constants having units of °C, °C, and hPa, respectively. Information on these coefficients is presented in **Table 1**.

Table 1. Coefficients in Eq. (2).

Coefficient	Unit	Value
T_1	°C	0.27
A_1	°C	0.37

https://doi.org/10.5194/amt-2021-246
Preprint. Discussion started: 28 September 2021

P_1	hPa	102.7

3.2 Effect of temperature

The following T values are used in the test chamber: −67 °C, −55 °C, −40 °C, −20 °C, 0 °C, and 20 °C. As shown in Fig. 2(a), ΔT_{rad} gradually increases as the temperature reduces in the pressure range of 5−50 hPa. This phenomenon likely occurs because the long-wave radiation from the temperature sensor reduces as the absolute temperature decreases. In addition, the cooling of the sensor may become less effective as the thermal conductivity of air decreases at low temperatures.

To incorporate the temperature effect in Eq. (1), the coefficients are fitted with empirical linear functions, as follows:

$$T_0(T) = a_0 \cdot T + a_1 \, , \quad (3)$$

$$A_0(T) = b_0 \cdot T + b_1 \, , \quad (4)$$

$$P_0(T) = c_0 \cdot T + c_1 \, , \quad (5)$$

where a_0, a_1, b_0, b_1, c_0, and c_1 are fitting coefficients. Information regarding these coefficients is summarized in **Table 2**.

Table 2. Coefficients in Eqs. (3), (4), and (5).

Coefficient	Unit	Value
a_0		-3.64×10^{-4}
a_1	°C	4.81×10^{-1}
b_0		-1.76×10^{-3}
b_1	°C	5.92×10^{-1}
c_0	hPa·°C^{-1}	-1.56×10^{-2}
c_1	hPa	1.31×10^{1}

The residuals obtained using Eqs. (1) and (2) and the associated fitting coefficients listed in **Table 1** and **2** are presented in Fig. 2(c). The fitted values agree with the measurement data within ±0.04 °C.

3.3 Estimation of the low temperature effect

The effect of low temperature on ΔT_{rad} is represented by the ratio (%) of ΔT_{rad} to the corresponding value at 20 °C (ΔT_{rad_20}), as shown in Fig. 3(a). The temperature effect ($\Delta T_{rad}/\Delta T_{rad\_20}$) gradually increases as the temperature and pressure decrease. $\Delta T_{rad}/\Delta T_{rad\_20}$ is 119% at T = –67 °C and P = 5 hPa. To obtain the information required to estimate the low temperature effect by using only ΔT_{rad} at 20 °C with varied P, ($\Delta T_{rad}/\Delta T_{rad\_20} \times 100$) is fitted with empirical linear functions:

$$\Delta T_{rad}/\Delta T_{rad\_20} \times 100 \text{ (\%)} = D(T) \cdot P + E(T) \quad (6)$$

https://doi.org/10.5194/amt-2021-246
Preprint. Discussion started: 28 September 2021

Atmospheric Measurement Techniques Discussions
Open Access EGU

where $D(T)$, represented in hPa^{-1}, and $E(T)$, which is dimensionless, are fitting coefficients with functions of T. $D(T)$ and $E(T)$ are fitted by linear functions of T, as follows:

$$D(T) = d_0 \cdot T + d_1 \,, \tag{7}$$

$$E(T) = e_0 \cdot T + e_1 \,, \tag{8}$$

where d_0, d_1, e_0, and e_1 are fitting coefficients. The information regarding these coefficients is summarized in **Table 3**.

Table 3. Coefficients in Eq. (7) and (8).

Coefficient	Unit	Value
d_0	$hPa^{-1} \cdot °C^{-1}$	2.74×10^{-3}
d_1	hPa^{-1}	-2.69×10^{-2}
e_0	$°C^{-1}$	-0.23×10^{0}
e_1		1.04×10^{2}

The residuals obtained using Eqs. (6), (7), and (8) are represented in Fig. 3(b). The estimated values agree with the measurement data within ±1.5% (left y-axis), corresponding to approximately ±0.01 °C (right y-axis). Using Eq. (6), the radiation correction for low temperatures can be estimated through only the room-temperature measurement.

3.4 Effect of ventilation speed

To investigate the effect of ascending speed of radiosondes, the air ventilation speed (v) in the test chamber is systematically varied in the range of 4−7 $m \cdot s^{-1}$. Figure 4(a) shows ΔT_{rad} as a function of the ventilation speed with the temperature varying from −67 °C to 20 °C. ΔT_{rad} decreases as the ventilation speed increases, primarily owing to the enhancement in the convective cooling. Because the pressure is fixed at 50 hPa, the temperature effect is clearly visible in Fig. 2(a). The measurement data at each temperature are fitted using a linear function (dashed lines) to formulate the effect of the ventilation speed. The slope of the linear functions indicates that an increase of 1 $m \cdot s^{-1}$ in v induces a decrease of 0.02–0.03 °C in ΔT_{rad}. Figure 4(b) shows ΔT_{rad} as a function of the ventilation speed with the pressure varying from 5 hPa to 300 hPa. The measurement data at each pressure are fitted using a linear function (dashed lines). The slopes are distributed from –0.04 °C/($m \cdot s^{-1}$) to –0.02 °C/($m \cdot s^{-1}$). Although the effect of the ventilation speed is coupled with the temperature and pressure effects, the coupling represented by the variation of slopes in Figs. 4(a) and (b) is minor in the range of 4−7 $m \cdot s^{-1}$. Therefore, the effect of the ventilation speed can likely be treated as an independent parameter. Thus, the ventilation effect is formulated considering the average slope in Figs. 4(a) and (b), which is –0.027 °C/($m \cdot s^{-1}$). This result is incorporated into Eqs. (1) and (2) at $v = 5\ m \cdot s^{-1}$:

$$\Delta T_{rad} = T_0(T) + A_0(T) \cdot \exp(-P/P_0(T)) - 0.027 \cdot (v\text{-}5) \text{ for } 5\text{ hPa} \le P \le 50\text{ hPa},\ S_0 = 980\ W \cdot m^{-2} \,, \tag{9}$$

$$\Delta T_{rad} = T_1 + A_1 \cdot \exp(-P/P_1) - 0.027 \cdot (v\text{-}5) \quad \text{for } 50\text{ hPa} < P < 500\text{ hPa},\ S_0 = 980\ W \cdot m^{-2} \,, \tag{10}$$

https://doi.org/10.5194/amt-2021-246
Preprint. Discussion started: 28 September 2021

The residuals obtained by applying Eqs. (9) and (10) are shown in Fig. 4(c). The fitted values agree with the measurement data within ±0.04 °C.

3.5 Effect of irradiation intensity

The linear relationship between ΔT_{rad} and the irradiance (S) is confirmed with reference to the existing studies based on theoretical and experimental approaches (Luers, 1990; Mcmillin et al., 1992; Lee et al., 2016). S is independent of T, P, and v. As previously observed, the variation of the other parameters results in a change in only the slope of the linear functions, and the linearity is not altered (Lee et al., 2018c; Lee et al., 2018b). Because all the experiments performed in this study adopt a fixed S_0 = 980 W·m^{-2} and the empirical fitting coefficients are accordingly obtained, the effect of the irradiation intensity can be incorporated into Eqs. (9) and (10) by using the linear relationship between ΔT_{rad} and S, as follows:

$$\Delta T_{rad} = S/S_0 \times [T_0(T) + A_0(T)\cdot\exp(-P/P_0(T)) - 0.027\cdot(v\text{-}5)] \quad \text{for } 5\text{ hPa} \leq P \leq 50\text{ hPa}, \quad (11)$$

$$\Delta T_{rad} = S/S_0 \times [T_1 + A_1\cdot\exp(-P/P_1) - 0.027\cdot(v\text{-}5)] \quad \text{for } 50\text{ hPa} < P < 500\text{ hPa}, \quad (12)$$

Consequently, Eqs. (11) and (12) can consider the radiation correction of the RS41 temperature sensor under simultaneously varying T, P, v, and S.

3.6 Effect of sensor boom rotation

The spinning motion of radiosondes during sounding is imitated by rotating the radiosonde in the test chamber, as shown in Fig. 1(d). The amplitude of the temperature oscillation is investigated by varying the rotation cycle (5 s, 10 s, and 15 s) under irradiation, as shown in Fig. 5(a). The maximum peak (T_{on_max}) and minimum peak (T_{on_mim}) appear alternately during the rotation. The difference between the peaks ($T_{on\_max} - T_{on\_min}$) increases with the rotation period. Each peak appears twice in a single cycle, as clearly observed in the 15 s cycle. This phenomenon occurs because the sensor boom undergoes similar processes in the first 180° and remaining 180° in a 360° rotation. The sensor boom experiences irradiation in the perpendicular and parallel directions at T_{on_max} and T_{on_min}, respectively. This finding suggests that the conductive heat transfer from the boom to the sensor influences T_{on_max}.

Figure 5(b) shows ($T_{on\_max} - T_{on\_min}$) as a function of pressure under different rotation cycles. The pressure effect is clearly visible when the rotation cycle is 15 s. Because the experiment is conducted at T = 25 °C, the effect of rotation at the lowest considered temperature (−67 °C) is estimated using Eqs. (6), (7), and (8). At P = 5 hPa, the value of ($T_{on\_max} - T_{on\_min}$) at −67 °C is 20% higher than that at 25 °C.

3.7 Effect of solar incident angle

The incident angle of irradiation to sensors primarily depends on the solar elevation angle and, during soundings, may also vary due to pendulum motion of the radiosonde. To investigate the effect of the solar incident angle, the sensor boom is tilted by θ with respect to the normal direction in the test chamber, as shown in Fig. 1(e). Figure 6(a) shows ΔT_{rad} as a function of

https://doi.org/10.5194/amt-2021-246
Preprint. Discussion started: 28 September 2021

pressure when the sensor boom is in the normal and tilted (θ = 27°) positions. ΔT_{rad} in the tilted position (red circle) is lower than that in the normal position (black square) because the effective irradiance (S_{eff}) is reduced by the tilting ($S_{eff} = S\times\cos 27°$). Because ΔT_{rad} is proportional to S_{eff}, the ratio $\Delta T_{rad\_tiled}/\Delta T_{rad\_normal}$ should be cosine 27°. The ratio roughly follows the theoretical value (blue dotted line). However, this value is slightly higher and lower than cosine 27° at pressure values less and more than 50 hPa, respectively. At higher pressures, this deviation can be explained by the effect of ventilation, which intensifies in the case of tilting of the sensor boom. However, the reason for the deviation from the theoretical value at low pressures remains unclear. In this paper, the effect of solar incident angle (or tilt angle, θ) is considered by using S_{eff} ($S\times\cos\theta$) and thus Eqs. (11) and (12) are revised into their final form as follows:

$$\Delta T_{rad} = (S_{eff}/S_0) \text{ x } [T_0(T) + A_0(T)\cdot\exp(-P/P_0(T)) - 0.027\cdot(v\text{-}5)] \quad \text{for } 5 \text{ hPa} \le P \le 50 \text{ hPa}, \tag{13}$$

$$\Delta T_{rad} = (S_{eff}/S_0) \text{ x } [T_1 + A_1\cdot\exp(-P/P_1) - 0.027\cdot(v\text{-}5)] \quad \text{for } 50 \text{ hPa} < P < 500 \text{ hPa}, \tag{14}$$

Figure 6(b) shows the difference between ΔT_{rad_tilted} and $\Delta T_{rad\_normal}\times\cos 27°$ as a function of the pressure. Because the experiment is conducted at T = 25 °C, the effect of the solar incident angle at the lowest considered temperature (−67 °C) is estimated using Eqs. (6), (7), and (8). At P = 5 hPa, ($\Delta T_{rad\_tilted} - \Delta T_{rad\_normal}\times\cos 27°$) at −67 °C is 20% higher than that at 25 °C. This value is used for the uncertainty due to the tilting of sensor boom in Section 4.7.

4 Uncertainty

4.1 Uncertainty factors

The uncertainty factors that contribute to the uncertainty budget of the radiation correction are summarized in **Table 4**, in addition with the experimental ranges considered in this work.

Table 4. Uncertainty factors and experimental ranges considered in this work.

Figure	T (°C)	P (hPa)	v (m·s^{-1})	S (W·m^{-2})	Position/Motion
2	–67 to 20	5–500	5	980	Normal
4(a)	–67 to 20	50	4–7	980	Normal
4(b)	–40	5–300	4–7	980	Normal
5	25	5–500	5	980	360° Rotation
6	25	5–500	5	980	27° Tilted

4.2 Uncertainty in the temperature, $u(T)$

The temperature of the test chamber is measured using a PRT installed in a shaded area. The PRT is calibrated at KRISS, and the calibration uncertainty is 0.025 °C with the coverage factor k = 1. The resistance of the PRT is measured using a digital multimeter calibrated at KRISS. Moreover, the stability of the temperature measured using the PRT is considered in determining $u(T)$. The uncertainty components and their contributions to $u(T)$ are listed in **Table 5**.

Table 5. Uncertainty budget for the test chamber temperature.

Uncertainty component	Contribution (°C)
Calibration of the PRT	0.025
Calibration of the multimeter	0.010
Stability of temperature measurement	0.007
$u(T)$, k = 1	0.028

4.3 Uncertainty in the pressure, $u(P)$

The pressure of the test chamber is measured using three pressure gauges for different pressure ranges. The gauges are calibrated at KRISS, and the calibration uncertainty is considered in determining $u(P)$. Moreover, the stability of the pressure measured using each pressure gauge is considered to determine $u(P)$. The uncertainty components and their contributions to $u(P)$ are listed in **Table 6**.

Table 6. Uncertainty budget for the test chamber pressure.

Uncertainty component	Pressure range (hPa)	Contribution (hPa)
Calibration of the pressure gauge	0−10	0.007
	10−100	0.08
	100−1000	0.1
Stability of pressure measurement	0−10	0.005
	10−100	0.11
	100−1000	0.14
$u(P)$, k = 1	0−10	0.01
	10−100	0.14
	100−1000	0.18

4.4 Uncertainty in the ventilation speed, $u(v)$

The SI traceability of the ventilation speed in the test chamber of the UAS is ensured by calibrating the sonic nozzles at KRISS. The calibration uncertainty of the sonic nozzles is 0.09 % (k = 1). The stability of the ventilation speed in the test chamber is considered to determine $u(v)$. The spatial gradient of the ventilation speed in the test chamber is measured through laser Doppler velocimetry at KRISS. The uncertainty components and their contributions to $u(v)$ are summarized in **Table 7**.

Atmospheric Measurement Techniques Discussions

Table 7. Uncertainty budget for the ventilation speed in the test chamber.

Uncertainty component	Contribution (m·s^{-1})
Calibration of sonic nozzles	0.005
Stability	0.052
Spatial gradient	0.026
$u(v)$, k = 1	0.058

4.5 Uncertainty in the irradiance, $u(S)$

The irradiance in the test chamber is measured using a pyranometer. The pyranometer is calibrated at KRISS, and the calibration uncertainty is 9.8 W·m^{-2} at k = 1. The stability of the irradiance measured using the pyranometer is considered to determine $u(S)$. In addition, the two-dimensional spatial uniformity of the irradiance in the test chamber is measured by moving the pyranometer. The spatial gradient is within ±5%, and a rectangular probability distribution is assumed for the uncertainty calculation. The uncertainty components and their contributions to $u(S)$ are summarized in **Table 8**.

Table 8. Uncertainty budget for the irradiance in the test chamber.

Uncertainty component	Contribution (W·m^{-2})
Calibration of pyranometer	9.8
Stability	6.0
Spatial gradient	28.3
$u(S)$, k = 1	30.5

4.6 Uncertainty due to sensor rotation

Since the sensor boom position for $T_{\mathrm{on\_max}}$ during the rotation corresponds to the normal position, the uncertainty due to sensor rotation is obtained based on ($T_{\mathrm{on\_max}} - T_{\mathrm{on\_min}}$), as shown in Fig. 5(b). The value estimated for T = –67 °C and P = 5 hPa is used to include sufficient uncertainty. The values are assumed to have a rectangular distribution, and thus, the corresponding standard uncertainty (k = 1) is obtained considering the maximum value (0.06 °C) divided by $\sqrt{3}$. Consequently, the uncertainty due to sensor rotation is 0.035 °C (k = 1).

4.7 Uncertainty due to tilting of the sensor

The uncertainty due to tilting of sensor boom is obtained using ($T_{\mathrm{on\_tilted}} - T_{\mathrm{on\_normal}}$·cos 27°) shown in Fig. 6(b). The value estimated for T = –67 °C and P = 5 hPa is used to include sufficient uncertainty. The values are assumed to have a rectangular

https://doi.org/10.5194/amt-2021-246
Preprint. Discussion started: 28 September 2021

distribution, and thus, the corresponding standard uncertainty (k = 1) is obtained considering the maximum value (0.045 °C) divided by $\sqrt{3}$. Consequently, the uncertainty due to sensor rotation is 0.026 °C (k = 1).

4.8 Uncertainty due to fitting error

Because Eqs. (13) and (14) are used for radiation correction, the residuals shown in Figs. 2(c) and 4(c) must be considered in determining the uncertainty. The residuals are assumed to have a rectangular distribution, and thus, the corresponding standard uncertainty (k = 1) is obtained considering the maximum absolute value divided by $\sqrt{3}$. Consequently, the uncertainty due to the fitting error is 0.025 °C (k = 1).

4.9 Uncertainty budget for radiation correction

The uncertainties in T, P, v, and S contribute to the uncertainty in the radiation correction by the uncertainty propagation law based on Eqs. (13) and (14):

$$\frac{\partial \Delta T_{\mathrm{rad}}}{\partial T} \cdot u(T)\ , \tag{15}$$

$$\frac{\partial \Delta T_{\mathrm{rad}}}{\partial P} \cdot u(P)\ , \tag{16}$$

$$\frac{\partial \Delta T_{\mathrm{rad}}}{\partial v} \cdot u(v)\ , \tag{17}$$

$$\frac{\partial \Delta T_{\mathrm{rad}}}{\partial S} \cdot u(S)\ , \tag{18}$$

where $u(\text{parameter})$ represents the standard uncertainty in each parameter at k = 1, and the partial differential terms represent the sensitivity coefficients. The sensitivity coefficients of the uncertainties due to sensor rotation, tilting of the sensor, and fitting error are 1 because they directly contribute to the uncertainty in the radiation correction. The uncertainty budget for the radiation correction (ΔT_{rad}) based on the conducted experiments is presented in **Table 9**.

Table 9. Uncertainty budget on the radiation correction (ΔT_{rad}).

Uncertainty factor	Condition	Unit	Standard uncertainty (k = 1)	Contribution to uncertainty of radiation correction (k = 2)
T	-67	°C	0.028	0.000 °C
P	5	hPa	0.01	0.000 °C
v	5	$\mathrm{m \cdot s^{-1}}$	0.058	0.004 °C
S	980	$\mathrm{W \cdot m^{-2}}$	30.5	0.062 °C
Rotation	24	$\mathrm{° \cdot s^{-1}}$	-	0.070 °C
Tilting	27	°	-	0.052 °C
Fitting error	-0.036 – 0.042	°C	0.025	0.051 °C
Expanded uncertainty of radiation correction (k = 2)				0.119 °C

https://doi.org/10.5194/amt-2021-246
Preprint. Discussion started: 28 September 2021

4.10 Uncertainty budget for the corrected temperature, T_{cor}

The corrected temperature (T_{cor}) is obtained by subtracting ΔT_{rad} from the raw temperature (T_{raw}), as follows:

$$T_{cor} = T_{raw} - \Delta T_{rad} \ . \tag{19}$$

Thus, the uncertainty in the corrected temperature, $u(T_{cor})$ is calculated as follows:

$$u(T_{cor})^2 = u(T_{raw})^2 + u(\Delta T_{rad})^2 \ , \tag{20}$$

where $u(T_{raw})$ is the standard uncertainty in the raw temperature (k = 1). The uncertainty in ΔT_{rad}, indicated in **Table 9**, must be rescaled in proportion to the actual solar irradiance for Eq. (20). Therefore, the uncertainty in ΔT_{rad} is scaled up to a level of solar constant (~1360 W·m^{-2}) by a factor of (1360/980) based on the linear relationship between ΔT_{rad} and S.
The calibration uncertainty associated with the temperature sensor must be considered to account for the uncertainty in the raw temperature. Consequently, the expanded uncertainty in the corrected temperature of RS41 is 0.193 °C (k = 2), as indicated in **Table 10**. The calibration uncertainty in the RS41 temperature sensor is specified by the manufacturer (Vaisala).

Table 10. Uncertainty budget for the corrected temperature.

Uncertainty factor	Uncertainty (k = 2)
Expanded uncertainty for the radiation correction at 1360 W·m^{-2}	0.165 °C
Calibration of RS41 temperature sensor	0.100 °C
Expanded uncertainty in the corrected temperature (k = 2)	0.193 °C

4.11 Comparison of RS41 radiation correction specified by Vaisala and that obtained through the UAS

Table 11. Radiation correction of RS41 by the Vaisala (Vaisala) and the UAS using Eq. (13) and (14).

	Radiation correction by Vaisala (v = 6 m·s^{-1})			Radiation correction by the UAS (v = 6 m·s^{-1}, S = 1360 W·m^{-2})			
Pressure (hPa)	Solar angle = 0°	Solar angle = 45°	Solar angle = 90°	T = 20 °C, θ = 45°	T = -67 °C, θ = 45°	T = -67 °C, θ = 27°	T = -67 °C, θ = 0°
1000	0.00 °C	0.10 °C	0.11 °C	0.24 °C	0.24 °C	0.30 °C	0.34 °C
500	0.03 °C	0.17 °C	0.19 °C	0.24 °C	0.24 °C	0.31 °C	0.34 °C
200	0.09 °C	0.29 °C	0.32 °C	0.29 °C	0.29 °C	0.37 °C	0.41 °C
100	0.16 °C	0.42 °C	0.45 °C	0.38 °C	0.38 °C	0.48 °C	0.54 °C
50	0.24 °C	0.58 °C	0.62 °C	0.45 °C	0.49 °C	0.62 °C	0.69 °C
20	0.39 °C	0.85 °C	0.90 °C	0.55 °C	0.64 °C	0.81 °C	0.90 °C
10	0.53 °C	1.10 °C	1.16 °C	0.69 °C	0.81 °C	1.02 °C	1.15 °C
5	0.68 °C	1.39 °C	1.45 °C	0.81 °C	0.96 °C	1.21 °C	1.36 °C

The radiation correction of RS41 by the UAS is based on Eqs. (13) and (14) for different pressure ranges. Although the conditions for the UAS correction are different from those considered by the manufacturer, a rough comparison of the radiation corrections is presented in **Table 11**. For the UAS correction, the solar irradiance is assumed to be S = 1360 W·m^{-2} at all pressure values. Depending on the effective irradiance (S_{eff}), the UAS correction value should be revised in a proportional manner using Eqs. (13) and (14).

5 Conclusions

The UAS developed at KRISS provides a unique opportunity to correct the solar radiation effect on commercial radiosondes by reproducing the environments that may be encountered by radiosondes by simultaneously controlling T, P, v, and S. The following ranges of T, P, and v are considered in this study: –67 °C to 20 °C, 5−500 hPa, and 4−7 m·s^{-1}, respectively, with a fixed S_0 = 980 W·m^{-2}. The functionalities of rotating and tilting the sensor boom are added considering the previous report on the UAS (Lee et al., 2020) to investigate the effect of the radiosonde motions with respect to the solar irradiation direction during ascent. The correction formula for the radiation effect on a Vaisala RS41 temperature sensor is derived through a series of experiments with varying environmental parameters and motions/positions of the radiosonde sensor. In addition, an empirical formula is derived to estimate the low temperature effect by using only the inputs of room-temperature measurements. The uncertainty associated with the radiation correction is evaluated by combining the contribution of each uncertainty factor. The uncertain factors considered for the radiation correction are T, P, v, and S as well as the sensor rotation, sensor tilting, and data-fitting-induced errors. The uncertainty budget for the radiation correction of RS41 temperature sensor is 0.119 °C at k = 2. When the uncertainty in the absolute temperature measurement (calibration uncertainty) is included, the uncertainty in the corrected temperature is estimated to be 0.193 °C at k = 2. The radiation correction values by the UAS are provided when the solar constant (1360 W·m^{-2}) is used for S for the comparison with those by the manufacturer. The radiation correction by the UAS depends on effective solar irradiance. Thus, the measurement of solar irradiance in situ and the calculation of effective irradiance are desirable to reflect the conditions such as clouding, solar elevation angle, and radiosonde movement, thereby obtaining more accurate correction values. To measure the solar irradiance in situ, a radiosonde model using dual temperature sensors with different emissivity values has been already tested using the UAS. The temperature difference in the two sensors of the radiosonde is used to measure solar irradiance in situ.

As the UAS can support wired and wireless data acquisition, it can be used for any type of commercial radiosonde to derive the radiation correction along with the corresponding uncertainty. Therefore, the UAS can help enhance the measurement accuracy of commercial radiosondes within the framework of the SI traceability.

Aknowledgement

This work was supported by the Korea Research Institute of Standards and Science under the grant GP2021-0005-02.

Author contribution

SL analysed the experimental data and wrote the manuscript. SK and YL conducted experiments. BC built the humidity control system, WK and YO built the air flow control system, and SP and JY established the solar simulator setup. SL and SK developed the measurement software. YK designed the experiments.

Competing interests

The authors declare that they have no conflicts of interest.

Data availability

The datasets generated and/or analyzed for this work are available from the corresponding author on reasonable request.

References

Choi, H. M., Park, K.-A., Oh, Y. K., and Choi, Y. M.: Uncertainty evaluation procedure and intercomparison of bell provers as a calibration system for gas flow meters, Flow Measurement and Instrumentation, 21, 488-496, https://doi.org/10.1016/j.flowmeasinst.2010.07.002, 2010.

Dirksen, R., Sommer, M., Immler, F., Hurst, D., Kivi, R., and Vömel, H.: Reference quality upper-air measurements: GRUAN data processing for the Vaisala RS92 radiosonde, Atmospheric Measurement Techniques, 7, 4463-4490, https://doi.org/10.5194/amt-7-4463-2014, 2014.

GCOS: GCOS Reference Upper-Air Network (GRUAN): Justification, requirements, siting and instrumentation options, Available at: https://library.wmo.int/doc_num.php?explnum_id=3821 [Accessed 5th August 2021], 2007.

ISO: Measurement of Gas Flow by Means of Critical Flow Venturi Nozzles, Available at: https://www.iso.org/obp/ui/#iso:std:iso:9300:ed-2:v1:en,

Lee, S. W., Choi, B. I., Kim, J. C., Woo, S. B., Park, S., Yang, S. G., and Kim, Y. G.: Importance of air pressure in the compensation for the solar radiation effect on temperature sensors of radiosondes, Meteorological Applications, 23, 691-697, https://doi.org/10.1002/met.1592, 2016.

Lee, S. W., Kim, S., Choi, B. I., Woo, S. B., Lee, S., Kwon, S., and Kim, Y. G.: Calibration of RS41 humidity sensors by using an upper-air simulator, Meteorological Applications, 28, e2010, https://doi.org/10.1002/met.2010, 2021.

Lee, S. W., Park, E. U., Choi, B. I., Kim, J. C., Woo, S. B., Park, S., Yang, S. G., and Kim, Y. G.: Correction of solar irradiation effects on air temperature measurement using a dual-thermistor radiosonde at low temperature and low pressure, Meteorological Applications, 25, 283-291, https://doi.org/10.1002/met.1690, 2018a.

Lee, S. W., Park, E. U., Choi, B. I., Kim, J. C., Woo, S. B., Park, S., Yang, S. G., and Kim, Y. G.: Dual temperature sensors with different emissivities in radiosondes for the compensation of solar irradiation effects with varying air pressure, Meteorological Applications, 25, 49-55, https://doi.org/10.1002/met.1668, 2018b.

Lee, S. W., Park, E. U., Choi, B. I., Kim, J. C., Woo, S. B., Kang, W., Park, S., Yang, S. G., and Kim, Y. G.: Compensation of solar radiation and ventilation effects on the temperature measurement of radiosondes using dual thermistors, Meteorological Applications, 25, 209-216, https://doi.org/10.1002/met.1683, 2018c.

https://doi.org/10.5194/amt-2021-246
Preprint. Discussion started: 28 September 2021

Lee, S. W., Yang, I., Choi, B. I., Kim, S., Woo, S. B., Kang, W., Oh, Y. K., Park, S., Yoo, J. K., and Kim, J. C.: Development of upper air simulator for the calibration of solar radiation effects on radiosonde temperature sensors, Meteorological Applications, 27, e1855, https://doi.org/10.1002/met.1855, 2020.

Luers, J. K.: Estimating the temperature error of the radiosonde rod thermistor under different environments, Journal of Atmospheric and Oceanic Technology, 7, 882-895, https://doi.org/10.1175/1520-0426(1990)007<0882:ETTEOT>2.0.CO;2, 1990.

McMillin, L., Uddstrom, M., and Coletti, A.: A procedure for correcting radiosonde reports for radiation errors, Journal of Atmospheric and Oceanic Technology, 9, 801-811, https://doi.org/10.1175/1520-0426(1992)009<0801:APFCRR>2.0.CO;2, 1992.

Philipona, R., Kräuchi, A., Romanens, G., Levrat, G., Ruppert, P., Brocard, E., Jeannet, P., Ruffieux, D., and Calpini, B.: Solar and thermal radiation errors on upper-air radiosonde temperature measurements, Journal of Atmospheric and Oceanic Technology, 30, 2382-2393, https://doi.org/10.1175/JTECH-D-13-00047.1, 2013.

Schmidlin, F. J., Luers, J. K., and Huffman, P.: Preliminary estimates of radiosonde thermistor errors, Available at: https://ntrs.nasa.gov/api/citations/19870002653/downloads/19870002653.pdf [Accessed 6th August 2021]. 1986.

Vaisala: Vaisala Radiosonde RS41 Measurement Performance, Available at: file:///C:/Users/%EC%9D%B4%EC%83%81%EC%9A%B1/Downloads/WEA-MET-RS41-Performance-White-paper-B211356EN-B-LOW-v3%20(1).pdf [Accessed 3rd August 2021].

https://doi.org/10.5194/amt-2021-246
Preprint. Discussion started: 28 September 2021

Atmospheric Measurement Techniques Discussions

Figure captions

Figure 1: Photographs of the (a) upper air simulator (UAS) and (b) test section with a radiosonde (Vaisala, RS41). Schematics of the radiosonde in the UAS at (a) normal, (b) rotating, and (c) tilted positions.

Figure 2: Temperature rise ($\triangle T_{rad}$) in a RS41 temperature sensor due to irradiation as a function of the air pressure in the range of (a) 5–50 hPa and (b) 50–500 hPa. (c) Residuals as a function of air pressure when Eqs. (1) and (2) are used.

Figure 3: (a) Effect of temperature on $\triangle T_{rad}$ normalized by that at 20 °C ($\triangle T_{rad\_20}$ = 100%) and (b) residuals of linear fittings as a function of the air pressure.

Figure 4: Effect of ventilation speed on $\triangle T_{rad}$ at (a) P = 50 hPa at different temperatures and (b) T = –40 °C at different air pressure values. (c) Residuals as a function of the ventilation speed when Eqs. (9) and (10) are used.

Figure 5: (a) Effect of sensor rotation with varied cycles (5 s, 10 s, and 15 s) and (b) difference in the maximum and minimum temperature values ($T_{on\_max} - T_{on\_min}$) as a function of the air pressure. $T_{on\_max} - T_{on\_min}$ at 100 hPa and 5 hPa at –67 °C are estimated using Eqs. (6), (7), and (8).

Figure 6. (a) Effect of tilting of the sensor boom showing (left y-axis) $\triangle T_{rad}$ with normal ($\triangle T_{rad\_normal}$) and 27° tilted position ($\triangle T_{rad\_tilted}$) and the ratio between them (right y-axis). (b) Residual between $\triangle T_{rad\_tilted}$ and $\triangle T_{rad\_normal}$×cos 27° at T = 25 °C and the estimate of the residual at T = -67 °C by using Eqs. (6), (7), and (8).

https://doi.org/10.5194/amt-2021-246
Preprint. Discussion started: 28 September 2021

Atmospheric Measurement Techniques Discussions

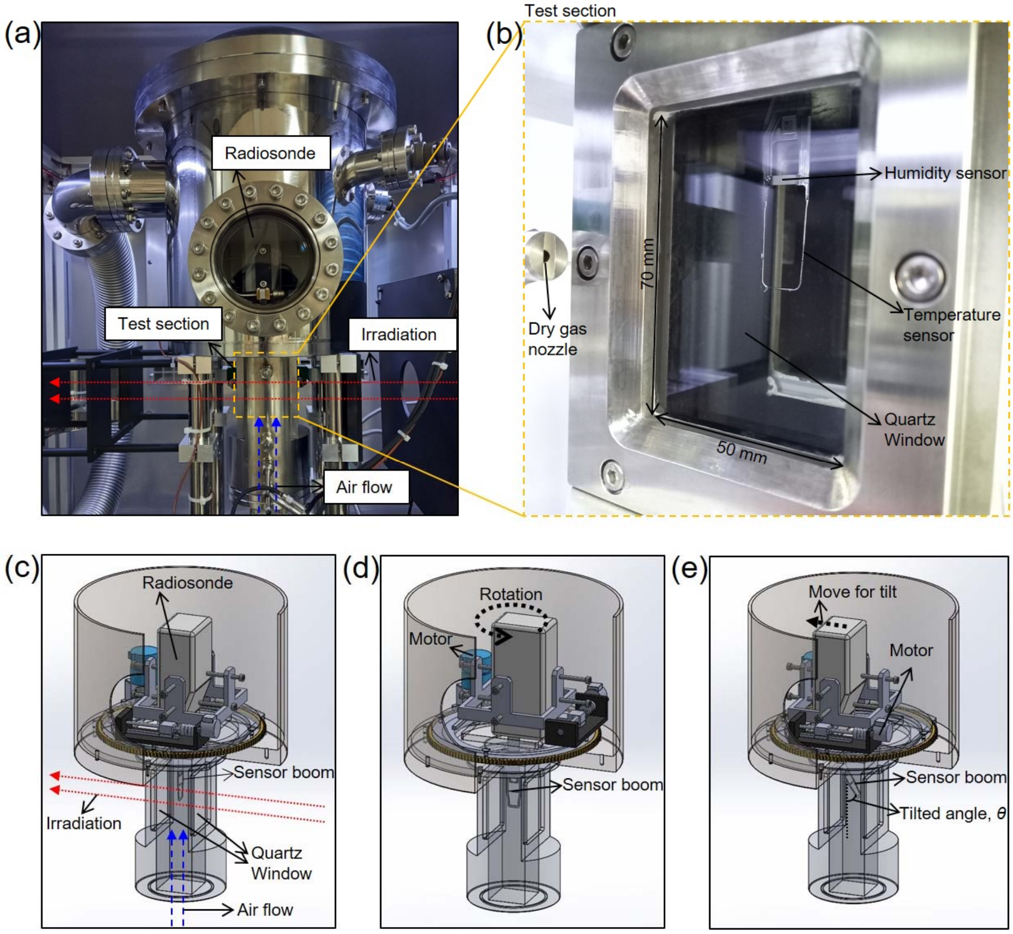

405
406 **Figure 1.** Photographs of the (a) upper air simulator (UAS) and (b) test section with a radiosonde (Vaisala, RS41). Schematics
407 of the radiosonde in the UAS at (a) normal, (b) rotating, and (c) tilted positions.

408

https://doi.org/10.5194/amt-2021-246
Preprint. Discussion started: 28 September 2021

Atmospheric Measurement Techniques
Discussions

409

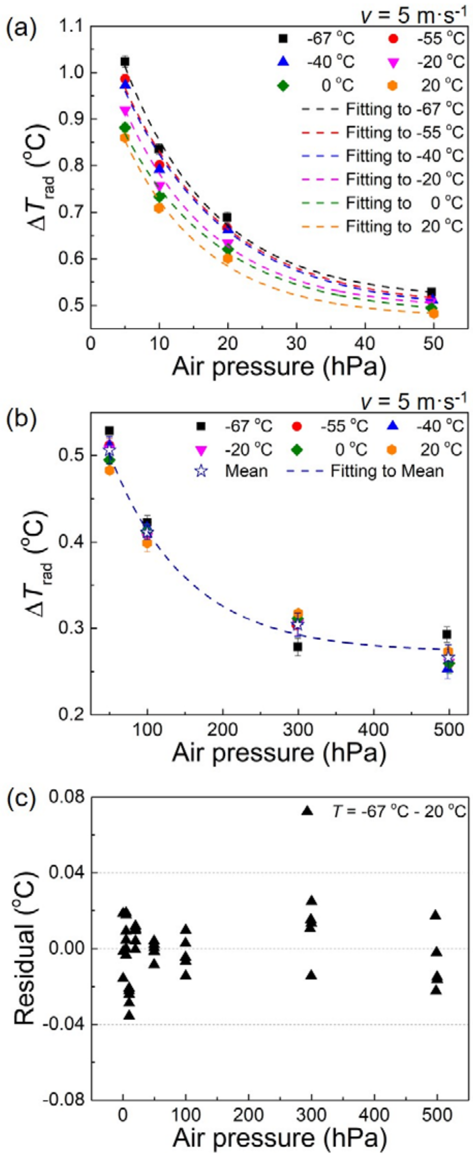

410 **Figure 2**. Temperature rise ($\triangle T_{rad}$) in a RS41 temperature sensor due to irradiation as a function of the air pressure in the range
411 of (a) 5–50 hPa and (b) 50–500 hPa. (c) Residuals as a function of air pressure when Eqs. (1) and (2) are used.

412

https://doi.org/10.5194/amt-2021-246
Preprint. Discussion started: 28 September 2021

Atmospheric Measurement Techniques
Discussions

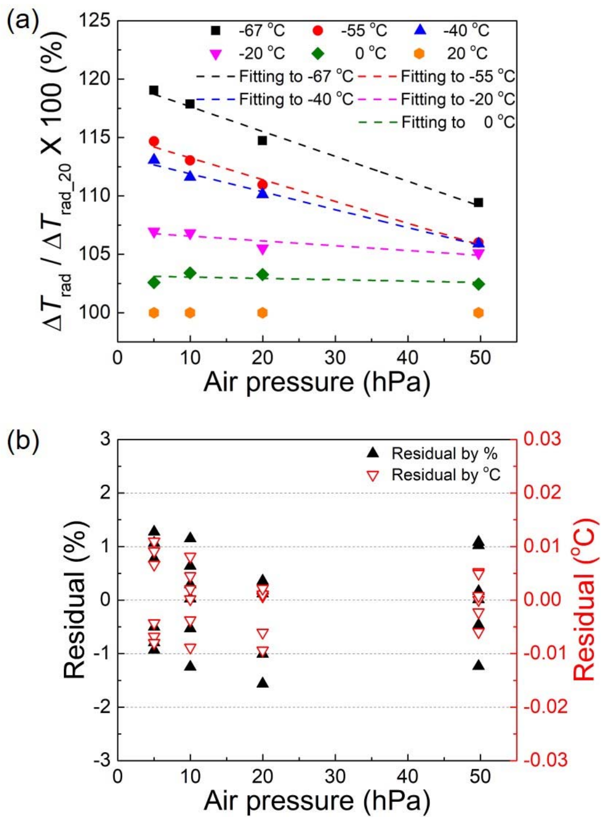

Figure 3. (a) Effect of temperature on $\triangle T_{rad}$ normalized by that at 20 °C ($\triangle T_{rad\_20}$ = 100%) and (b) residuals of linear fittings as a function of the air pressure.

https://doi.org/10.5194/amt-2021-246
Preprint. Discussion started: 28 September 2021

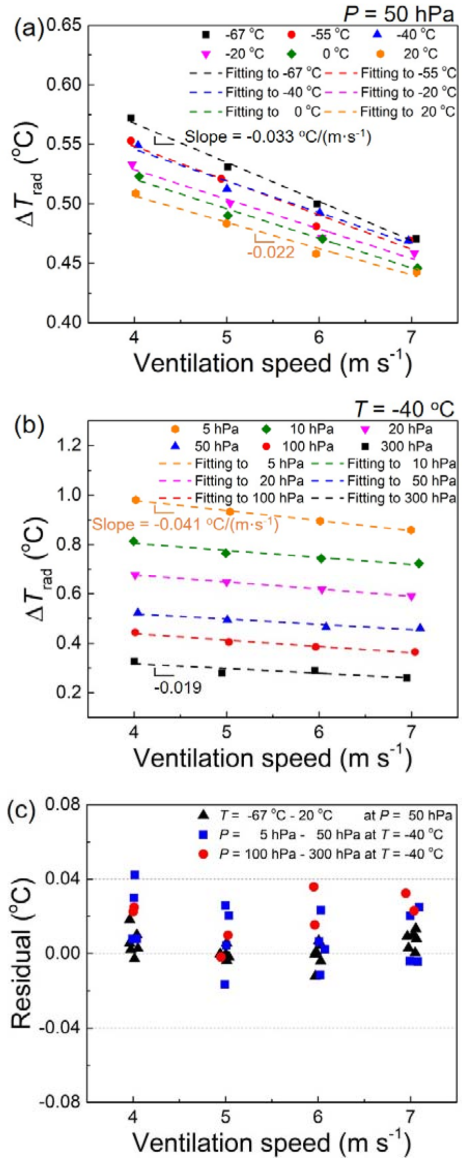

Figure 4. Effect of ventilation speed on ΔT_{rad} at (a) P = 50 hPa at different temperatures and (b) T = –40 °C at different air pressure values. (c) Residuals as a function of the ventilation speed when Eqs. (9) and (10) are used.

https://doi.org/10.5194/amt-2021-246
Preprint. Discussion started: 28 September 2021

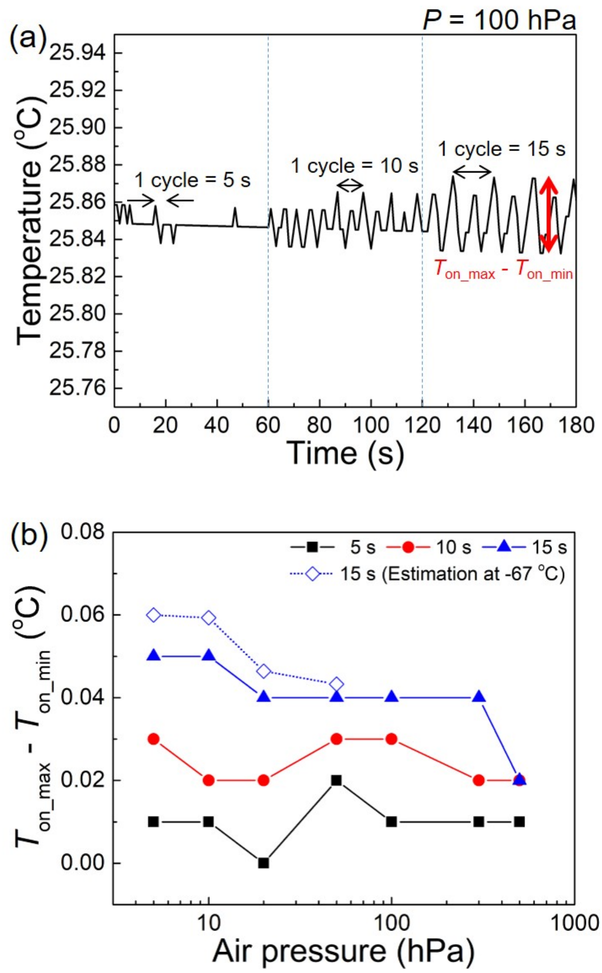

Figure 5. (a) Effect of sensor rotation with varied cycles (5 s, 10 s, and 15 s) and (b) difference in the maximum and minimum temperature values ($T_{on\_max} - T_{on\_min}$) as a function of the air pressure. $T_{on\_max} - T_{on\_min}$ at 100 hPa and 5 hPa at –67 °C are estimated using Eqs. (6), (7), and (8).

https://doi.org/10.5194/amt-2021-246
Preprint. Discussion started: 28 September 2021

Atmospheric Measurement Techniques
Discussions

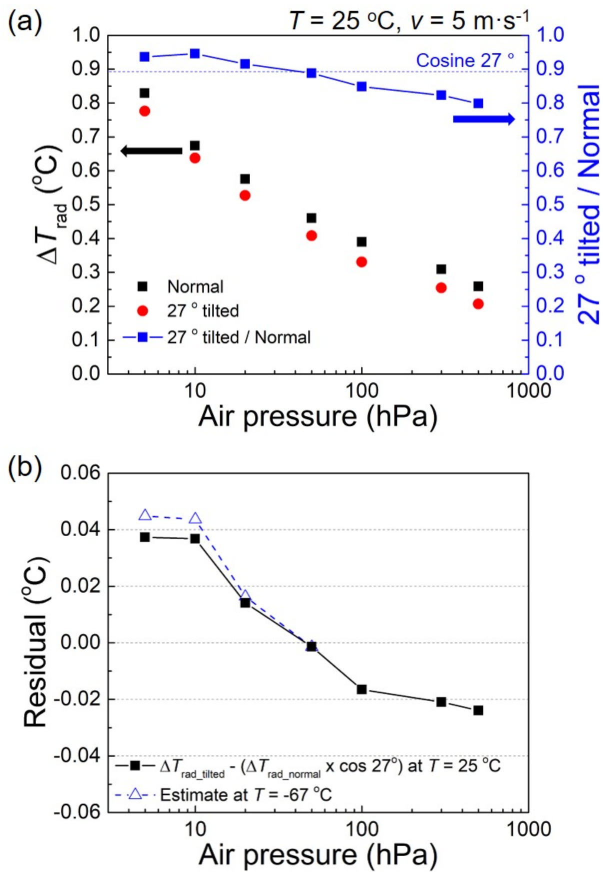

Figure 6. (a) Effect of tilting of the sensor boom showing (left y-axis) ΔT_{rad} with normal (ΔT_{rad_normal}) and 27° tilted position (ΔT_{rad_tilted}) and the ratio between them (right y-axis). (b) Residual between ΔT_{rad_tilted} and $\Delta T_{rad\_normal}\times\cos 27°$ at T = 25 °C and the estimate of the residual at T = -67 °C by using Eqs. (6), (7), and (8).